Experimental Verification of Open-Switch Fault Localization in a Six-Switch Three-Phase PMSM Drive Inverter

Dominik Łuczak
Poznan University of Technology, Poznan, Poland
Email: dominik.luczak@put.poznan.pl
ORCID: 0000-0002-2755-5503

***Abstract*—This paper presents an experimental verification of a convolutional neural network (CNN)-based method for open-switch fault localization in a six-switch three-phase (6S3P) inverter supplying a permanent magnet synchronous motor (PMSM). Three-phase current signals (1024 samples per phase) are converted into compact 32×32×3 RGB image representations using a sliding-window signal-to-image encoding that preserves temporal and inter-phase relationships. Two normalization strategies, namely per-channel and common normalization, are evaluated to assess their impact on classification performance. The method is validated on laboratory data covering six open-switch faults and three operating speeds (60, 70, and 80 rad/s), with training performed at a reference speed 70 rad/s and testing conducted on unseen conditions (60, and 80 rad/s). The results demonstrate 100% fault-phase localization accuracy for the common-normalization variant, confirming strong generalization across the tested speed range. The proposed CNN-based pipeline provides an effective fault-localization stage that can support fault-tolerant reconfiguration from the 6S3P to the 4S3P topology.**

***Index Terms*—open-switch fault, PMSM, inverter fault localization, CNN, 6S3P, 4S3P, RGB signal representation.**

I. Introduction

Power electronic converters in PMSM drives are vulnerable to semiconductor and gate-driver malfunctions. An open-switch fault introduces strong current asymmetry and may destabilize the control system unless it is detected and localized rapidly. In safety-critical and availability-critical applications, the inverter can continue operating in a fault-tolerant 4S3P topology, provided that the faulty phase is identified reliably.

Traditional fault-localization methods are often based on handcrafted features computed in the time or frequency domain. Although effective in selected operating ranges, such features may be sensitive to operating-point changes and often require domain-specific tuning. In contrast, image-based signal representations combined with convolutional neural networks can learn discriminative spatial patterns directly from measured waveforms without manual feature engineering, which is consistent with broader advances in deep learning and representation learning reported in the literature [1]–[3].

This research was funded in whole by National Science Centre, Poland 2024/53/B/ST7/01308.

Recent studies also report robust open-circuit fault diagnosis across different converter structures, including charging modules, back-to-back converters, dual-inverter PMSM drives, NPC converters, and multi-leg inverter systems [4]–[9]. These results motivate further research on data-driven methods that retain high diagnostic reliability under varying operating conditions.

This paper experimentally verifies a CNN-based fault-localization approach using real laboratory data from a 6S3P inverter-fed PMSM drive. The main contribution is the validation of a signal-to-image encoding pipeline and CNN classifier that achieve perfect localization accuracy across multiple operating speeds, including previously unseen test conditions.

II. Fault-Tolerant Control Context

The PMSM drive normally operates with a healthy 6S3P inverter. When an open-switch fault is detected, the hardware transitions to a fault-tolerant 4S3P configuration. Proper reconfiguration requires precise identification of the affected phase (A, B, or C), because the modulation scheme and switch assignment depend directly on the faulty branch.

The modulation-side background for fault-tolerant PMSM operation and space-vector-based reconfiguration has been investigated in earlier studies [10], [11].

The proposed localization module acts as a supervisory subsystem that provides the faulty phase index to the reconfiguration logic. This enables continued drive operation under constrained post-fault conditions.

III. Fault Localization Method

The localization pipeline converts the phase currents $i_a(t)$, $i_b(t)$, and $i_c(t)$ into compact RGB images used for CNN classification.

A. Signal-to-Image Encoding

The localization chain, shown in Fig. 1, uses a sliding window of 1024 samples, which corresponds to 51.2 ms at the sampling frequency of 20 kHz ($T_s = 50\,\mu$s). Each window is reshaped into a 32×32 matrix, and the three phase currents are assigned to the red, green, and blue image channels, respectively, which yields a 32×32×3 RGB representation. Consecutive windows are shifted by 32 samples (1.6 ms), resulting in 96.875% overlap. The primary reason for this high overlap is to minimise the phase shift between the window content and the moment of fault onset, ensuring that each window captures a complete and well-centred fault signature rather than a truncated or transitional one. A consequence of this design choice is a higher correlation between adjacent windows, which should be acknowledged when interpreting validation metrics.

B. Normalization Strategies

Before reshaping, the window samples are normalized to the range $[0, 1]$. Two strategies are compared:

- **Per-channel normalization**: each phase current channel is independently rescaled using its own minimum and maximum within the window. This emphasizes intra-phase waveform shape, but removes inter-phase amplitude relations.
- **Common normalization**: all three channels are jointly rescaled using the global minimum and maximum of the entire window. This preserves amplitude asymmetry across phases, which is a characteristic signature of open-switch faults.

Figure 1 illustrates the processing chain and contrasts the two normalization variants used for training and evaluation.

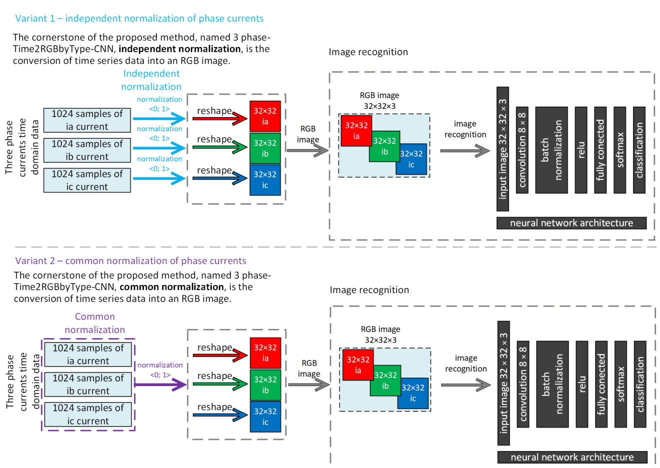

Fig. 1. Signal-to-image processing variants used in this work: (a) per-channel normalization of i_a, i_b, and i_c before RGB mapping, and (b) common normalization over all three phase currents within the same 1024-sample window.

The resulting RGB representation preserves temporal relationships between the phase currents in a compact two-dimensional structure, and the selected normalization strategy determines how much inter-phase amplitude information is retained for the convolutional layers to exploit.

IV. Experimental Setup

Open-switch faults corresponding to the upper and lower switches in phases A, B, and C were experimentally injected in a PMSM drive laboratory stand. Data were sampled at 20 kHz for 30 s at each operating speed, which yielded 600,000 samples per phase and operating point.

A. Data Volume

After sliding-window segmentation and signal-to-image conversion, one single-fault case at one reference speed yields 3094 RGB images. Aggregating all six single-fault cases (S1–S6) results in 18,564 images for one reference speed. Three operating speeds, namely 60, 70, and 80 rad/s, were considered, which gives a total dataset size of 55,692 images. Training and validation were performed using the 70 rad/s subset, while the 60 rad/s and 80 rad/s subsets were treated as unseen test data in order to verify speed generalization capability within the tested range. This speed-disjoint split reduces train-test leakage between operating points. The high overlap is intentional — it minimises the phase shift between the window and the fault event — but it does introduce strong local correlation among adjacent windows inside each subset, which should be kept in mind when interpreting the reported accuracy.

B. Hardware Platform

The laboratory setup used for data acquisition is shown in Fig. 2. In a previous stage of the investigation, both the standard 6S3P operating mode and the fault-tolerant 4S3P operating mode were successfully validated on the same bench, as detailed in [12]. The rig is equipped with the ALFINE-TIM ALS-G3-1369 controller board based on the Analog Devices SHARC ADSP-21369 digital signal processor and the ALFINE-TIM three-phase inverter LABINVERTER P3-5.0/550MFE. The power stage supplies the blue PMSM drive visible in the photograph. Tables I and II summarize the acquisition parameters and PMSM characteristics.

The project was executed using a Lenovo ThinkPad P16 Gen 2 workstation with a QHD display, equipped with an Intel Core i7-14700HX processor featuring 20 cores (8 P-cores and 12 E-cores, 28 threads), 128 GB RAM, and two 1 TB storage drives. The system incorporated an NVIDIA RTX 3500 GPU with 5120 CUDA cores and 12 GB GDDR6 memory, providing hardware-accelerated computation, and operated on Windows 11 Pro.

TABLE I
Verification Summary

Item	Value	Description
Data length	600,000	30 s at 20 kHz
Window length	1024	51.2 ms
Window shift	32	1.6 ms
Images per case	3094	one fault case
Images per speed	18,564	all six cases
Train/validation set	70 rad/s	0.8/0.2 split
Test set	60, 80 rad/s	37,128 images total

For localization, each 1024-sample segment is mapped to one RGB image of size 32×32×3. The dataset includes examples of faults in all three phases and both switch positions.

Representative short time-series fragments used in the study are shown in Fig. 3. The collage illustrates the measured signal

Fig. 2. Laboratory setup used for experimental verification, including the DSP/FPGA based LabInverter platform, the PMSM drive, and the workstation used for supervision and data acquisition.

TABLE II
PMSM PARAMETERS

Parameter	Value
Rated power	0.75 kW
Rated speed	1500 rpm (≈157.08 rad/s)
Encoder	14-bit absolute encoder

patterns for cases labelled normal and S4 at the reference speed of 70 rad/s.

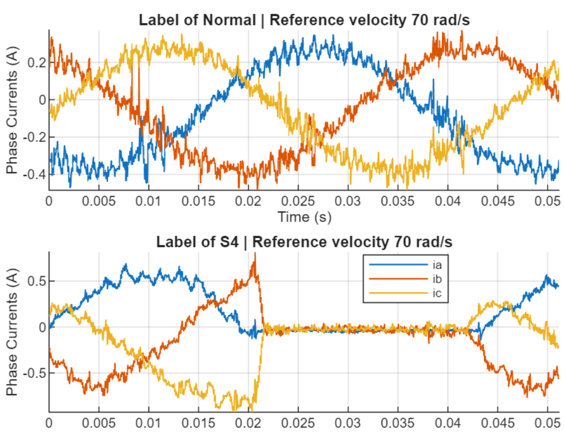

Fig. 3. Representative short time-series collage for cases normal and S4 at the reference speed of 70 rad/s.

V. RESULTS AND DISCUSSION

The CNN achieved 100% classification accuracy for the common-normalization strategy across training, validation, and unseen test speeds. The reported performance was obtained with training and validation at 70 rad/s and testing on the unseen 60 rad/s and 80 rad/s operating points, which indicates strong generalization across the considered speed range. Representative confusion matrices are shown in Figs. 4–7. This behavior is aligned with recent reports on robust data-driven open-circuit diagnosis under varying operating conditions [4]–[9].

Figures 4 and 5 present the confusion matrices obtained for the per-channel normalization variant, while Figs. 6 and 7 correspond to the common-normalization variant. In all four cases, the dominant values are concentrated on the main diagonal, which confirms correct assignment of the fault-phase class and indicates negligible inter-class confusion. The comparison between training and test matrices further shows that performance is preserved under unseen speed conditions, supporting the generalization capability of the proposed classifier. The common-normalization variant achieved perfect accuracy on the validation and test sets, while the per-channel normalization variant showed slightly lower performance, which suggests that preserving inter-phase amplitude relationships provides more discriminative features for the CNN to learn; this observation is also coherent with physically informed converter-fault studies that emphasize inter-phase signatures [6], [8], [11].

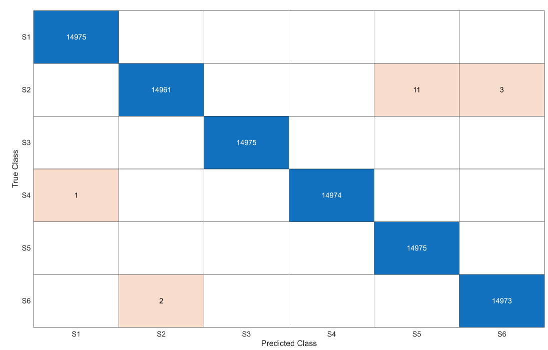

Fig. 4. Training confusion matrix for the per-channel normalization variant.

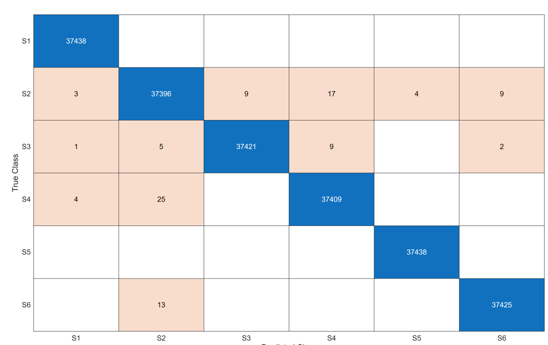

Fig. 5. Test confusion matrix for the per-channel normalization variant.

Representative short current waveforms are shown in Fig. 8. The collage presents cases normal and S4 for the reference

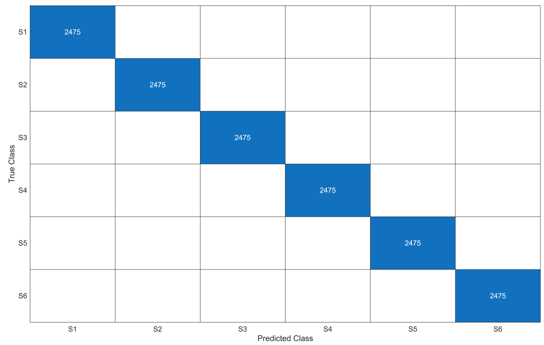

Fig. 6. Training confusion matrix for the common-normalization variant.

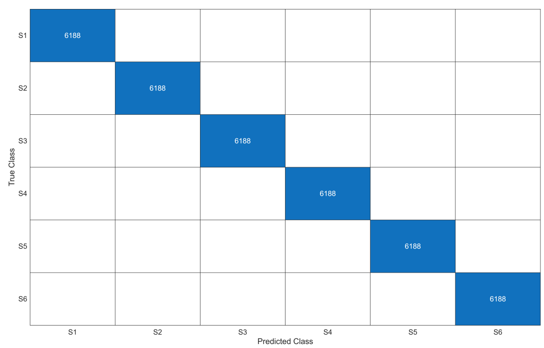

Fig. 7. Test confusion matrix for the common-normalization variant.

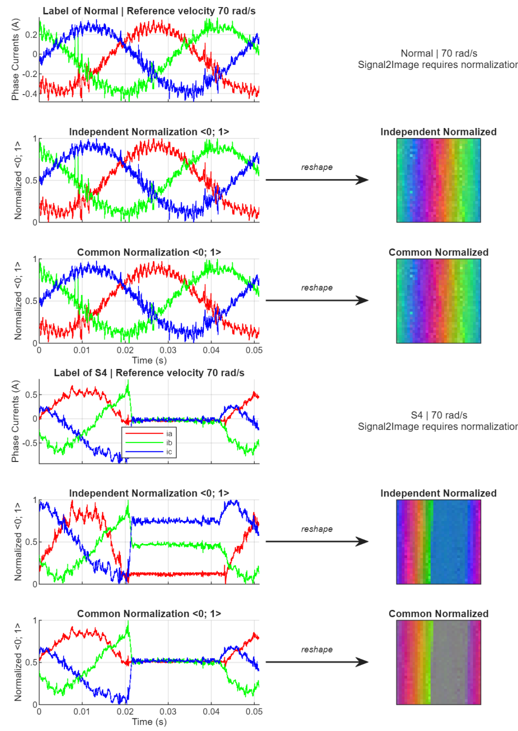

Fig. 8. Representative short current time-series collage for cases normal and S4 at the reference speed of 70 rad/s, shown in the context of the signal-to-image preprocessing stage.

speed of 70 rad/s and illustrates the temporal patterns used for RGB image generation. The normal case shows balanced three-phase currents, while the S4 case exhibits clear asymmetry in the affected phase, which is a key signature exploited by the CNN for accurate fault localization. The method was examined across all six single-fault cases and three operating speeds, and the results consistently showed perfect localization performance under these conditions. Case normal corresponds to the healthy condition, while cases S1–S6 correspond to open-switch faults in the upper and lower switches of phases A, B, and C, respectively. In this study, the classifier is designed for fault localization among fault classes rather than for end-to-end healthy/fault detection and diagnosis.

A. Training Behaviour

Figure 9 compares the training progress of both normalization strategies and shows stable convergence throughout the learning process. The common normalization variant achieved perfect accuracy on the validation set after 150 iterations, while the per-channel normalization variant converged slightly slowly and did not reach perfect accuracy within the same number of epochs. This observation suggests that preserving inter-phase amplitude relationships through common normalization provides more discriminative features for the CNN to learn, which leads to faster convergence and better generalization performance in line with established deep-learning representation principles [1], [2].

Training was performed in MATLAB Deep Learning Toolbox using the stochastic gradient descent with momentum optimizer. Execution was forced on GPU, and the built-in training-progress plot was used for monitoring.

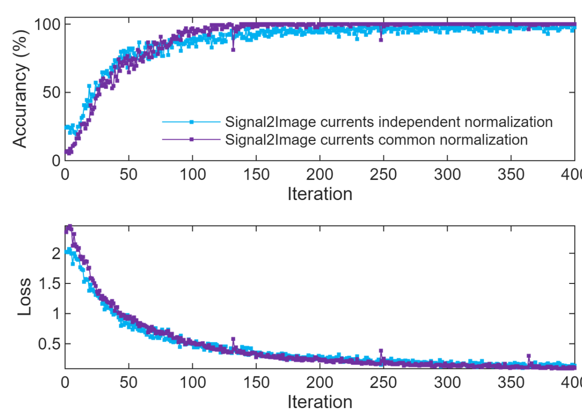

Fig. 9. Training progress for both normalization variants.

B. CNN Explainability

Class activation maps shown in Figs. 10 and 11 indicate that the CNN focuses on waveform regions in which amplitude asymmetry emerges, which is consistent with the physical signature of open-switch faults. In particular, the most activated regions are concentrated around intervals where one phase departs from the expected three-phase balance and where the inter-phase relation changes rapidly, i.e., exactly where fault-dependent information is most discriminative. The identified regions are consistent with diagnostic mechanisms discussed in prior PMSM and inverter fault studies [6], [8], [13].

The activation distributions also provide qualitative evidence that the network does not rely on irrelevant background patterns of the RGB representation. Instead, the attention is localized on physically meaningful structures linked to the faulted branch behavior. For the common-normalization variant, the highlighted regions are typically more compact and contrastive, which is coherent with preserved inter-phase amplitude relations and with the stronger classification performance observed in the confusion matrices. Overall, the explainability analysis supports that the classifier decisions are aligned with known converter-fault mechanisms rather than spurious correlations.

C. Comparison to Traditional Classifiers

Compared with feature-based classical classifiers such as decision trees, support vector machines, and k-nearest neighbors, prior evidence in [13] suggests that RGB+CNN representations can provide higher and more consistent localization accuracy. This observation suggests that spatially structured image embeddings capture fault-related patterns more effectively than handcrafted feature vectors, which is in agreement with recent open-circuit diagnosis studies using advanced learning-based models [4], [6], [9]. In the present work, all experiments were focused on validating the proposed RGB+CNN pipeline, and direct re-implementation of classical baselines and simpler deep-learning alternatives under an identical protocol is left for future work. Such a controlled benchmark will be important to quantify the incremental benefit of the proposed representation and network design.

D. Scope, Validation Protocol, and Practical Limitations

The reported results should be interpreted within the tested operating envelope and protocol. First, the very high overlap between adjacent windows (96.875%, shift of 32 samples / 1.6 ms) is a deliberate design choice to minimise the phase shift between the window content and the actual fault event, thereby ensuring that each image captures a complete fault signature. As a consequence, adjacent windows are highly correlated, so the reported accuracy figures should be read in the context of this redundancy even though a speed-disjoint train/test split was applied. Second, generalization has been verified only across the three tested speed values, so claims should be limited to this range until additional operating conditions (e.g., different torque levels, load disturbances, and parameter drifts) are included.

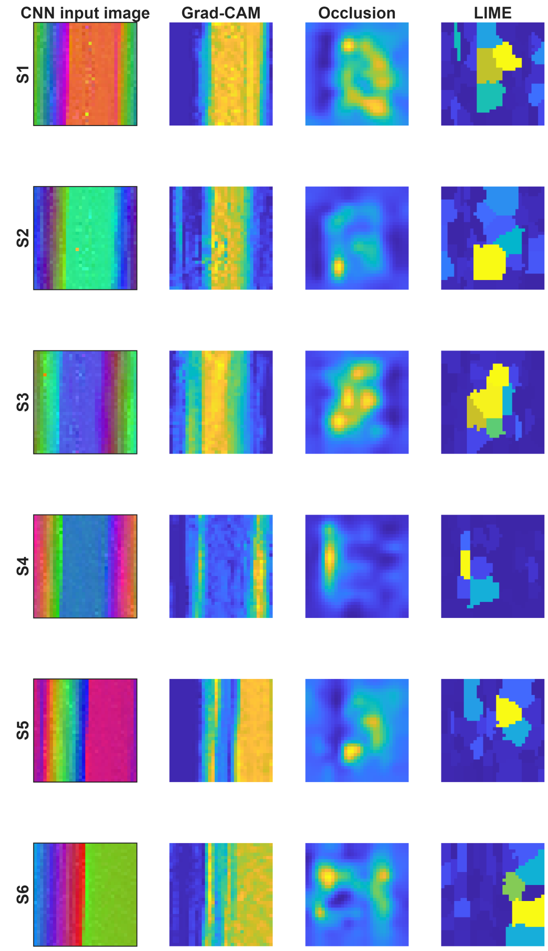

Fig. 10. Explainability map for the per-channel normalization variant.

Third, the present module addresses fault localization after fault occurrence and does not constitute a complete healthy/fault diagnosis pipeline. Fourth, while the method appears suitable for supervisory use, explicit real-time applicability should be supported by deployment-oriented measurements such as end-to-end latency per window, throughput, memory footprint, and embedded-target execution time. Finally, given the perfect accuracy values, robustness would be further strengthened by repeated training runs with different random seeds and by tests under slightly perturbed conditions (measurement noise, sensor offset, and minor timing jitter).

VI. Conclusion

This paper experimentally validates a CNN-based approach for localizing open-switch faults in a 6S3P inverter using RGB images of three-phase currents. The method with common

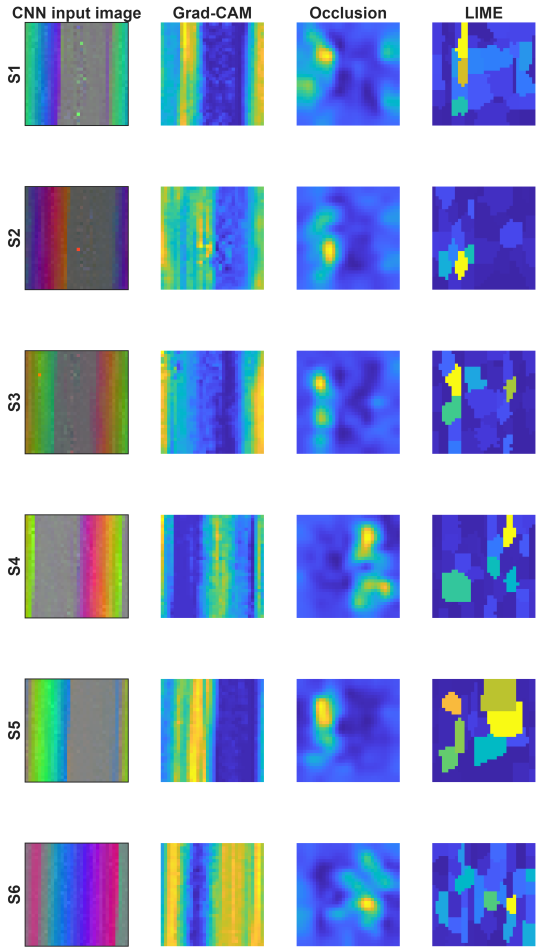

Fig. 11. Explainability map for the common normalization variant.

normalization preserves temporal and amplitude relationships across phases and achieves 100% accuracy for the tested protocol, including unseen speeds within the considered range. These findings support the potential of the RGB+CNN pipeline as a localization module for supervisory fault-tolerant reconfiguration to the 4S3P topology after fault detection. The common-normalization strategy is recommended because it retains inter-phase amplitude information that is critical for accurate fault localization. The explainability analysis confirms that the CNN focuses on physically meaningful regions of the input representation, which supports the reliability of the classification decisions.

Future work will extend the approach to intermittent and multi-switch faults, include additional operating conditions, provide direct comparisons with classical and lightweight deep-learning baselines under the same protocol, report explicit inference-time and deployment metrics, and perform robustness analyses with repeated runs and perturbed measurements.

Data Availability

The dataset used in this study will be publicly available on Zenodo [14] after the publication of this work.

Acknowledgment

This research was funded in whole by National Science Centre, Poland, grant no. 2024/53/B/ST7/01308. The author gratefully acknowledge the financial support provided the project entitled *"Step Towards Self-Aware Electric Drives"*, which made this study possible.

References

[1] Y. LeCun, Y. Bengio, and G. Hinton, "Deep learning," *Nature*, vol. 521, no. 7553, pp. 436–444, 2015, doi: 10.1038/nature14539.

[2] Y. Bengio, A. Courville, and P. Vincent, "Representation learning: A review and new perspectives," *IEEE Trans. Pattern Anal. Mach. Intell.*, vol. 35, no. 8, pp. 1798–1828, 2013, doi: 10.1109/TPAMI.2013.50.

[3] R. B. Randall and J. Antoni, "Rolling element bearing diagnostics—A tutorial," *Mech. Syst. Signal Process.*, vol. 25, no. 2, pp. 485–520, 2011, doi: 10.1016/j.ymssp.2010.07.017.

[4] Q. Guan, J. Hu, X. Hu, Y. Fan, Q. Cai, and X. Tan, "Open-circuit fault diagnosis for charging modules based on transfer light gradient boosting machine," *IEEE Open J. Power Electron.*, vol. 6, pp. 1759–1768, 2025, doi: 10.1109/OJPEL.2025.3620488.

[5] T. Ji, A. Lu, Y. Li, and L. Zhang, "Open-circuit fault diagnosis method of doubly-fed back-to-back converter based on mathematical morphology and fractional-order Hilbert transform," *Electr. Power Syst. Res.*, vol. 256, p. 112855, Jul. 2026, doi: 10.1016/j.epsr.2026.112855.

[6] C. Jiang, H. Liu, P. Wheeler, F. Wu, and J. Huo, "An open-circuit fault detection method of PMSM fed by dual inverter with high robustness," *IEEE Trans. Energy Convers.*, 2023, doi: 10.1109/TEC.2023.3263160.

[7] S. J. de la Rosa-Mendoza, R. Alvarez-Salas, M. A. Gonzalez-Garcia, and G. Espinosa-Perez, "Open-circuit switch fault diagnosis of an NPC converter in a DFIG-based WECS," *Electr. Power Syst. Res.*, vol. 252, p. 112410, Jan. 2026, doi: 10.1016/j.epsr.2025.112410.

[8] S. Xu, Y. Zhang, Y. Hu, *et al.*, "Multiple open-switch fault diagnosis for three-phase four-leg inverter under unbalanced loads via interval sliding mode observer," *IEEE Trans. Power Electron.*, vol. 39, no. 6, pp. 7607–7619, 2024, doi: 10.1109/TPEL.2024.3372650.

[9] G. Zhang, M. Li, X. Gu, and W. Chen, "Fault diagnosis method for open-circuit faults in NPC three-level inverter based on WKCNN," *CES Trans. Electr. Mach. Syst.*, vol. 9, no. 2, pp. 234–245, 2025, doi: 10.30941/CESTEMS.2025.00012.

[10] D. Łuczak and K. Siembab, "Comparison of fault tolerant control algorithm using space vector modulation of PMSM drive," in *Proc. 16th Int. Conf. Mechatronics*, 2014, pp. 24–31, doi: 10.1109/MECHATRONIKA.2014.7018231.

[11] K. Siembab and K. Zawirski, "Modified space vector modulation for fault tolerant control of PMSM drive," in *Proc. IEEE PEMC*, 2016, pp. 1064–1071, doi: 10.1109/EPEPEMC.2016.7752142.

[12] D. Łuczak, K. Nowopolski, K. Siembab, and B. Wicher, "PMSM laboratory stand for investigations on advanced structures of electrical drive control," in *Proc. 20th Int. Conf. Methods and Models in Automation and Robotics (MMAR)*, Aug. 2015, pp. 596–601, doi: 10.1109/MMAR.2015.7283942.

[13] D. Łuczak, S. Brock, and K. Siembab, "Fault detection and localisation of a 3-phase inverter with PMSM load using a convolutional neural network," *Actuators*, vol. 12, 2023, doi: 10.3390/act12030125.

[14] D. Łuczak and W. Nowacki, "PMSM Three Phase Currents Dataset for Single Open-Switch Fault Research at 60, 70, and 80 rad per second" Zenodo, Apr. 05, 2026, doi: 10.5281/zenodo.19424013.